
Characterizing Nonlinear Dynamics via Smooth Prototype Equivalences

Roy Friedman¹ Noa Moriel¹ Matthew Ricci¹ Guy Pelc¹ Yair Weiss¹ Mor Nitzan^{1,2,3}

Abstract

Characterizing dynamical systems given limited measurements is a common challenge throughout the physical and biological sciences. However, this task is challenging, especially due to transient variability in systems with equivalent long-term dynamics. We address this by introducing *smooth prototype equivalences* (SPE), a framework that fits a diffeomorphism using normalizing flows to distinct prototypes — simplified dynamical systems that define equivalence classes of behavior. SPE enables classification by comparing the deformation loss of the observed sparse, high-dimensional measurements to the prototype dynamics. Furthermore, our approach enables estimation of the invariant sets of the observed dynamics through the learned mapping from prototype space to data space. Our method outperforms existing techniques in the classification of oscillatory systems and can efficiently identify invariant structures like limit cycles and fixed points in an equation-free manner, even when only a small, noisy subset of the phase space is observed. Finally, we show how our method can be used for the detection of biological processes like the cell cycle trajectory from high-dimensional single-cell gene expression data.

1. Introduction

Predicting the long-term behavior of dynamical systems from sparse data is a challenging problem in data science and computational physics (Ghadami & Epureanu, 2022). The problem of identifying these behaviors, referred to as *invariant sets*, arises throughout the physical and life sciences. For example, in the early detection of dangerous self-excited oscillations in aeronautical design (Weisshaar, 2012; Dimitriadis, 2017) and in the classification of cell cycle

dynamics in computational biology (Chervov & Zinovyev, 2022; Moriel et al., 2023). Even if governing equations are known, there are few guarantees on the existence of long-term equilibrium or oscillatory behaviors (Hilbert, 1902; Smale, 2000), and this situation is exacerbated in realistic cases where equations are unknown and behavior must be estimated from sparse, noisy and/or high-dimensional data.

We construe this problem as a form of prototype learning, where long-term structures are identified and localized by comparison to archetypal class exemplars (Bonilla & Robles-Kelly, 2012). Prototype methods have their conceptual origin in cognitive science (Rosch, 1973) and have seen widespread use across machine learning applications, especially in service of few-shot learning (Chen et al., 2023). Here, we propose *smooth prototype equivalences* (SPE¹), a method that fits a diffeomorphism from the given data to so-called *normal forms* (Nayfeh, 2008), a natural choice for prototypes in the realm of dynamical systems. Normal forms are systems, $\dot{x} = g(x)$, whose governing equations take a mathematically concise form and which describe canonical dynamical behaviors. These normal forms are then the basis of equivalence classes $\{f_H\}_{H \in \mathcal{H}}$ of topologically identical dynamics via:

$$f_H(x) = \left(\frac{\partial H(x)}{\partial x} \right)^{-1} g(H(x)), \quad (1)$$

for a family of diffeomorphisms \mathcal{H} . In this case, we say that $f_H(\cdot)$ is smoothly equivalent to the prototype $g(\cdot)$. In particular, the action of H preserves the existence of invariant sets under the dynamics in both systems (e.g. fixed points, limit cycles, etc.). This means that the problem of characterizing and localizing the invariant set of a dynamical system given its measurements is reduced to that of identifying the prototype that is equivalent to it and mapping that prototype’s invariant structure to the data domain. Below, we demonstrate how this can be done by efficiently optimizing a diffeomorphism to such a prototype. When the equivalent prototype of the system is unknown, we classify the behavior according to the most similar prototype out of several candidates, resulting in a robust framework for long-term dynamical behavior which outperforms existing baselines.

¹School of Computer Science & Engineering ²Racah Institute of Physics ³Faculty of Medicine, The Hebrew University of Jerusalem. Correspondence to: Roy Friedman <roy.friedman@mail.huji.ac.il>, Mor Nitzan <mor.nitzan@mail.huji.ac.il>.

¹Code available in <https://github.com/nitzanlab/prototype-equivalences>.

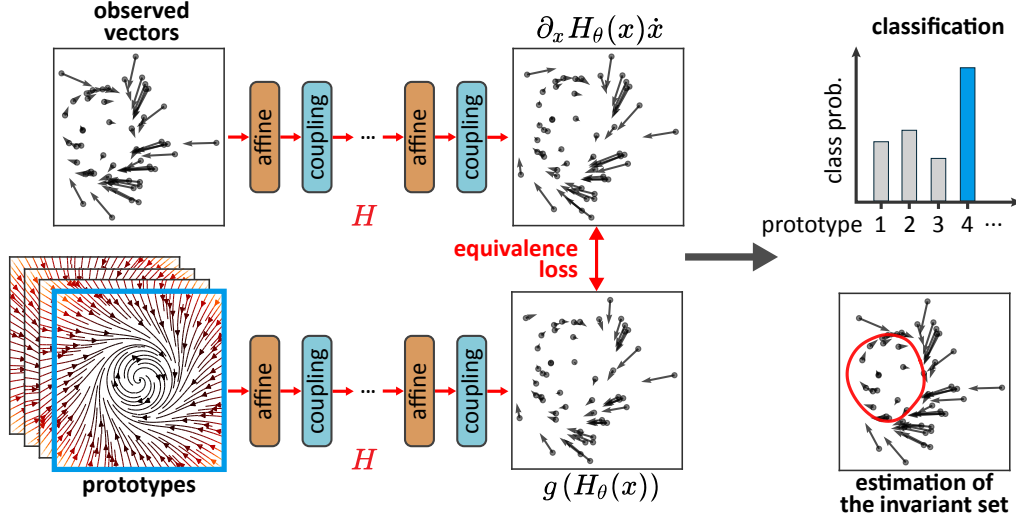


Figure 1. Schematic for the process of fitting dynamical prototypes using smooth prototype equivalences (SPE). The observed dynamics are compared to each of the chosen prototypes, which involves training a diffeomorphism $H_\theta(x)$, parameterized by a neural network, for each prototype $g(y)$. After training each of the diffeomorphisms, the observed dynamics are classified to the prototype with the smallest equivalence loss. Once the diffeomorphism $H_\theta(x)$ is trained, we have access to a mapping between the data space and the prototype space, which allows us to estimate the long-term behavior, i.e. invariant set, of the dynamics underlying the observed data.

Leveraging the fact that normalizing flows (Papamakarios et al., 2021) can approximate diffeomorphisms, $H \in \mathcal{H}$, we optimize normalizing flows which transform samples, (x, \dot{x}) , to a predefined prototype system. Our use of prototypes of pre-defined, simple dynamical structure means that we can easily use our optimized normalizing flows to locate invariant sets (i.e. limit cycles, fixed points) in complex samples with unknown governing equations. The minimal residual loss across parallel optimizations to candidate prototypes is used to make the classification decision, extending existing work on data-driven dynamical equivalence (Chen et al., 2024; Skufca & Bollt, 2008) to the classification domain. Importantly, we show how using normal forms as hardwired knowledge can greatly increase the robustness of classification to the sparse measurement and few-sample setting. Unlike earlier studies, we show how SPE can identify low-dimensional dynamics embedded in higher dimensional data, leading to a form of normalizing-flow-based model reduction.

We focus on data domains described by prototypes representing oscillatory dynamics. This is a key test case for both theoretical and practical reasons. On the theoretical front, sustained, isolated oscillations (i.e. limit cycles) are only possible in nonlinear systems and the problem of detecting and localizing these cycles is notoriously challenging (it is one of David Hilbert’s famous unsolved mathematical challenges (Hilbert, 1902)) even in systems with known, simple forms. On the practical front, the emergence of oscillations is of widespread importance in real-world nonlinear systems, particularly in engineering and biological applications.

We showcase SPE on oscillations in gene expression, a critical dynamical phenomenon for various biological functions (Novák & Tyson, 2008) whose dis-regulation has bearing on the proper function of cells and whole tissues, such as in the case of the runaway cell division in cancer (Suski et al., 2021; Ghafouri-Fard et al., 2022; Cavalu et al., 2024). Further, the sparsity of single-cell RNA-sequencing gene expression measurements as well as their high-dimensionality (providing information for the activity levels of tens-of-thousands of genes in thousands of cells simultaneously) makes this domain an important showcase for our framework (Bergen et al., 2021; Zheng et al., 2023).

Our concrete contributions include the following:

- *Efficient identification and localization of invariant structures from dynamical data.* By our novel synthesis of prototype methods with data-driven dynamical systems, we strongly regularize the challenging problem of dynamical classification, specifically in the paradigmatic case of oscillatory dynamics. We first demonstrate how SPE can efficiently identify invariant structures in a synthetic data set of two-dimensional oscillatory dynamical systems drawn from across the physical and life sciences. Further, the optimized normalizing flows used in prototype matching can be used to identify invariant structures in the sample data, despite the absence of closed-form governing equations. These results are then extended to higher-dimensional systems, situating SPE as a form of dynamical model reduction.

- *Systematic benchmarking for sparsity and data consumption.* Realistically, data is generated from time series measurements that are sparsely sampled. The robustness of the prototype method is further benchmarked under noisy conditions and small-data regime. This demonstrates the value of prototype matching in regularizing a challenging problem and justifies our method for use on real data.
- *Robust classification of gene expression dynamics.* We deploy our method on the detection of oscillations in gene expression dynamics, a domain where measurement sparsity and the curse of dimensionality make dynamical classification challenging. Using our extension to high dimensions, we are able to classify synthetic data of the six-dimensional repressilator gene regulatory network (Elowitz & Leibler, 2000).
- *Reconstruction of the cell cycle trajectory from single-cell gene expression and RNA velocities data.* Finally, we find a cyclic attractor, interpreted as the cell cycle, in the single-cell gene expression data of a proliferating cell population (Mahdessian et al., 2021). SPE stands out from alternative methods that either rely on the identity of key genes or on the distribution of the cells in gene expression space.

2. Related Works

Classical work on dynamical equivalence. Early notions of equivalence of dynamical systems are due to Poincaré (Poincaré, 1892–1899), who introduced foundational ideas like qualitative analysis of trajectories, periodic orbits, and invariant sets. Half a century later, Andronov & Pontryagin laid out conditions for two systems to be equivalent when differing by small, differentiable perturbations. A similar idea was put to use by independent work of Hartman and Grobman, who demonstrated that dynamical systems were topologically conjugate to their linearization near a hyperbolic fixed point, a result which was extended to the case of smooth conjugacy by Sternberg; Sternberg. Pre-saging the importance of discrete numerics in the current data-driven paradigm, the development of symbolic dynamics (Morse & Hedlund, 1938) demonstrated how to encode certain continuous-time trajectories as sequences of symbols, where topological conjugacy can be more easily detected. Later, Takens’ Embedding Theorem (Takens, 1981) expanded equivalence to high-dimensional systems, demonstrating that delay embeddings preserve topological conjugacy. These classical results provided important tools and conceptual frameworks for studying equivalence, but typically lacked a way to construct explicit conjugacies and often required explicit knowledge of governing equations, limiting their real-world usage.

Data-driven approaches to equivalence detection. Data-driven methods have sought explicit construction of conjugate mappings by defining graded notions of the otherwise binary concept of topological conjugacy. Building on Boltt and Skufca’s concept of “relaxed” conjugacy (Skufca & Boltt, 2007; 2008), recent work introduced DFORM (Chen et al., 2024) a method for learning diffeomorphisms between the vector fields of dynamical systems which uses a loss residual as a degree of conjugacy. Related works (Redman et al., 2022; Glaz, 2024) leverage the fact that conjugate systems have conjugate Koopman operators, using the linearity of these operators to speed up conjugacy detection. Bramburger et al. addressed a related problem whereby one learns a simpler, conjugate version of a discrete-time system via a deep neural network. These methods are predominantly concerned with comparing two specific vector fields, whose governing equations are frequently known, and are less suited to the discovery and categorization of specific topological structures within the vector fields. Moriel et al. took an empirical approach to the categorization of the invariant set in an observed vector field by training a deep network to distinguish random samples from two conjugacy classes representing oscillatory and non-oscillatory dynamics. This enables classification of systems when the underlying governing equations are hidden, but is restricted to conjugacy classes defined during the training of the network and the only information that can be extracted using this method is the class of the observed dynamics.

3. Method

3.1. System identification using smooth equivalence

Given a set of observations from a vector field $\mathcal{D} = \{(x_i, \dot{x}_i)\}_{i=1}^N$, we aim to classify these points as one of K prototype dynamical systems $\dot{y} = g_k(y)$ where y are the variables of the dynamical system, determined by the vector field $g_k(y)$. We do not have access to the underlying function describing the dynamics of the system $\dot{x} = f(x)$, but we assume that $f(x)$ is smoothly equivalent to one of the prototypes in the sense of Equation (1). Following DFORM (Chen et al., 2024), we can classify a sample by fitting K different diffeomorphisms $H_k : \mathcal{X} \rightarrow \mathcal{Y}$, using the following *equivalence loss*:

$$L_E(H_k, g_k) = \frac{1}{N} \sum_{i=1}^N \left\| \frac{\partial_{x_i} H_k(x_i) \dot{x}_i}{\|\partial_{x_i} H_k(x_i) \dot{x}_i\|} - \frac{g_k(H_k(x_i))}{\|g_k(H_k(x_i))\|} \right\|^2 \quad (2)$$

If this loss is equal to 0, then $f(x)$ and $g_k(y)$ are guaranteed to be smoothly equivalent. In practice, this loss will almost never be equal to zero, but it was shown that it provides a good indication of similarity between dynamical systems when there is access to a large amount of samples (Chen et al., 2024). We also found it beneficial to regularize the

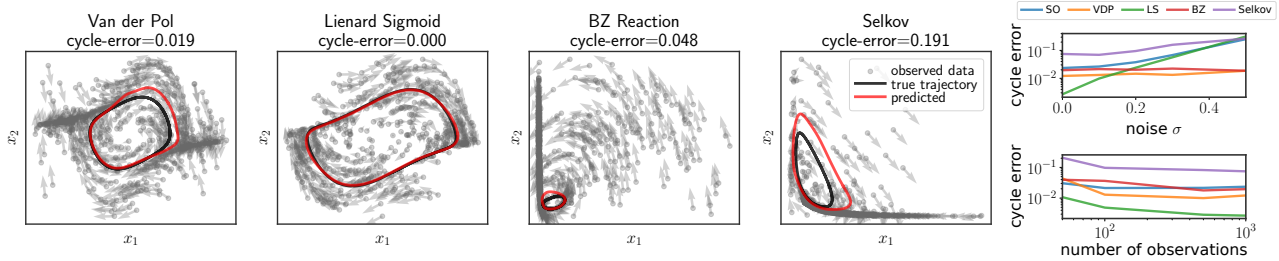


Figure 2. **Estimation of limit cycles using SPE for various 2D dynamical systems.** **Left:** examples of invariant sets predicted from the 500 observed vectors (in gray), for four different dynamical systems exhibiting a limit cycle attractor. For each system, a long ground-truth trajectory was simulated from the hidden system and plotted in black. The red curves are the limit cycles predicted using our method. **Right:** the average cycle-error of the different systems (simple oscillator (SO), Van der Pol (VDP), Liénard Sigmoid (LS), BZ reaction (BZ), and Selkov) as a function of the standard deviation of the noise (top) and number of observations (bottom).

average log-determinant of the Jacobian $\partial_x H_\theta(x)$ to be close to 0 and to ensure that the dynamics are centered around the mean of the data (see Appendix A.3 for more information). The full equivalence loss is thus given by:

$$L(H_k, g_k) = L_E(H_k, g_k) + \lambda_{\det} L_{\det}(H_k) + \lambda_{\text{cent}} L_{\text{cent}}(H_k) \quad (3)$$

where λ_{\det} and λ_{cent} are the regularization coefficients for the average determinant and centering of the diffeomorphism, respectively. A schematic of the classification process can be seen in Figure 1.

Normal form prototypes have simple functional forms and their invariant sets can be both identified (for example as fixed points, limit cycles or other attractors) and localized (for example with a closed mathematical form). This means that, after classification of a set of observations to their (approximately) smoothly equivalent normal form prototype, we can use the corresponding optimized diffeomorphism H_k to identify structures that are topologically equivalent in the real data, which are in general very difficult to find. This process would allow us to conclude, for example, that if a prototype, g , has a limit cycle, γ , then $H_\theta^{-1}(y)$ for $y \in \gamma$ is a limit cycle in the observed data.

Because we focus on the case of two-dimensional limit cycles (which can in general be embedded in higher dimensions), we can reduce to the use of only four prototype systems given in polar coordinates by:

$$\begin{aligned} \dot{r} &= r(a - r^2) \\ \dot{\theta} &= \omega. \end{aligned} \quad (4)$$

Here, a controls whether the system will exhibit a fixed point (negative values) or limit cycle (positive values), and ω determines the orientation of the cycle (clockwise when negative and counter-clockwise when positive). Importantly, the limit cycle is easily identified in this system: it is the circle of radius \sqrt{a} . Throughout the text, we refer to this system as the *simple oscillator* (SO).

3.2. Modeling diffeomorphisms with normalizing flows

In our setting, we only have access to the pairs (x, \dot{x}_i) and the prototype $g(y)$ (unlike DFORM which additionally assumes access to the governing equations $\dot{x} = f(x)$). This means that it is not possible to learn the reverse mapping $y \mapsto x$ during training, which is a crucial element in the training of the invertible ResNets (Behrmann et al., 2019) used in DFORM. Furthermore, to train the diffeomorphisms of DFORM, many batches of different points x are sampled to promote the convergence of the large ResNets that are used. On the other hand, in our setting the observed vectors from the vector field are restricted to a set collected from a hidden system, and therefore, as in many realistic settings, the observations might be extremely sparse. As such, instead of using the models suggested in DFORM, we opt to use more modestly-sized models whose inverse can be explicitly calculated.

In all of our experiments, we used normalizing flows (NFs, Papamakarios et al. 2021) as our parametric diffeomorphisms. NFs are a type of neural network composed of multiple invertible functions, $\ell_i(\cdot)$:

$$H_\theta(x) = \ell_L \circ \dots \circ \ell_1(x) \Leftrightarrow H_\theta^{-1}(y) = \ell_1^{-1} \circ \dots \circ \ell_L^{-1}(y) \quad (5)$$

Besides being invertible, NFs allow for efficient and explicit computations of both the log-determinants of the Jacobian of the diffeomorphism as well as the Jacobian-vector products (JVPs) needed in order to calculate the loss, $\partial_x H_k(x)\dot{x}$.

Our NFs utilize a relatively small number of blocks, composed of alternating invertible affine transformations and affine coupling layers (Dinh et al., 2014). Both of these layer types are adapted so that their JVPs can be calculated in closed form and to be low-weight. Specifically, instead of the typical multi-layer perceptrons (MLPs) in affine coupling layers (Papamakarios et al., 2021) we use cosine features, which we call *Fourier feature coupling*. These Fourier feature coupling layers are highly expressive while remain-

	SO	Aug. SO	Liénard Poly	Liénard Sigmoid	Van der Pol	BZ Reaction	Sel'kov	Attractor estimation
SPE	<u>0.97</u>	0.85	0.94	<u>0.89</u>	0.94	0.89	0.68	✓
TWA	0.98±0.01	0.93±0.01	<u>0.86±0.13</u>	0.92±0.07	<u>0.83±0.15</u>	<u>0.82±0.11</u>	<u>0.65±0.03</u>	x
Critical Points	0.54	0.56	0.70	0.49	0.56	0.84	0.51	x
Lyapunov	0.64	0.60	0.85	0.67	0.87	0.83	0.57	x
Phase2vec	0.73±0.08	0.71±0.04	0.49±0.06	0.48±0.0	0.49±0.04	0.50±0.0	0.49±0.0	x
Autoencoder	0.95±0.03	<u>0.87±0.01</u>	0.63±0.16	0.88±0.09	0.81±0.16	0.82±0.13	0.49±0.02	x

Table 1. Comparison of the classification accuracy of SPE to different models across various dynamical systems, when classifying between periodic and node dynamics. For each dynamical system, the classification accuracy is averaged over 100 instances of the system with different parameters (see Appendix B.1 for more details on the parameter settings). The observed vectors were positioned on a dense 64×64 grid, with the addition of Gaussian noise with a standard deviation of $\sigma = 0.1$ on the velocities. Where relevant, the standard deviations in accuracy are over different initializations. The highest scores for each column are shown in bold, with the second highest underlined.

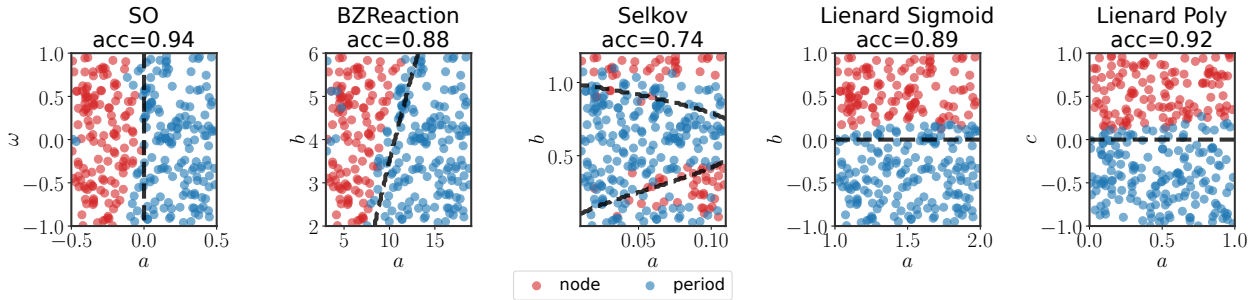


Figure 3. Classification of 2D dynamical systems between node and periodic attractors using SPE. Each point in the scatter represents dynamics from a realization of the different dynamical systems, under a specific choice of parameters defined by the x and y-axis of the plots, with $N = 1000$ observed vectors. Each of these was classified by SPE to either a node attractor (red) or periodic attractor (blue). The dashed black line depicts the ground truth bifurcation boundary between periodic and node dynamics. The classification accuracy using SPE, averaged over all parameters considered, is written at the top of each scatter plot.

ing narrow and shallow (one hidden layer whose width is smaller than 10), and their JVPs can be calculated in closed form without relying on autograd methods. For exact details, see Appendix A.

4. Results

4.1. Reconstructing attractors from sparse data

First, we demonstrate how diffeomorphisms optimized to match a dynamical prototype can be used to locate attractors in sparse data. This is a challenging problem since sparsity and noise make the underlying, unknown dynamical equations strongly undetermined. We demonstrate how SPE circumvents this difficulty on data simulated from four standard two-dimensional dynamical systems exhibiting limit cycles. The governing equations for these systems can be found in Appendix B.1.

To that end, we optimized a diffeomorphism, H_θ , between observed systems and a single limit cycle prototype (Equa-

tion (4), $a = \frac{1}{4}$, $\omega = \frac{1}{2}$) by minimizing the equivalence loss from Equation (2). Data from observed systems were acquired by first sampling N initial conditions which were used to generate numerical solutions on the interval $[0, T_{\max}]$ at a time resolution $\Delta t = 10^{-2}$. From these, we then sampled one vector, (x_i, \dot{x}_i) , uniformly from each trajectory, resulting in a data set, $\mathcal{D} = \{(x_i, \dot{x}_i)\}_{i=1}^N$, of $N = 1000$ vectors per system. More details on the simulations can be found in Appendix B.

After fitting H_θ to the observed data \mathcal{D} , we estimated the location of the limit cycle in data space by uniformly sampling a sequence of points, $T_y = \{y_j\}_{j=1}^M$, which lie along the limit cycle of the prototype in \mathcal{Y} . Each point was then mapped back into data space to define a trajectory along the estimated invariant set of the observed dynamics: $\hat{T}_\chi = H_\theta^{-1}(T_y) = \{H_\theta^{-1}(y_j)\}_{j=1}^M$. An example of predicted limit cycles can be seen in Figure 2 (left), where the black orbits are the true limit cycles of the observed vectors while the red orbits are the estimated locations of

the same limit cycles, based on the observed vectors. We observed a tight fit between predicted and true limit cycles in all four example systems (Figure 2). To further quantify the validity of the predicted limit cycles, we simulated a long trajectory $T_{\mathcal{X}}$ from the ground-truth (hidden) system, long enough to ensure that it arrived at the invariant set. We then transformed it into the prototype space using the learned diffeomorphism, $H_{\theta}(T_{\mathcal{X}})$. Each point on this trajectory was then compared to the closest point on the limit cycle of the attractor $y_i = \text{proj}_{\theta}(H_{\theta}(x_i))$, where $\text{proj}_{\theta}(x)$ returns the point closest to x on the limit cycle. These points are then transformed back into data space and their *cycle error* is defined as the mean squared error between these projections and the original points:

$$\text{cycle-error} = \frac{1}{|T_{\mathcal{X}}| \cdot \sigma_x^2} \sum_i \|x_i - H_{\theta}^{-1}(\text{proj}_{\theta}(H_{\theta}(x_i)))\|^2 \quad (6)$$

where $\sigma_x^2 = \text{var}\{\{x \in T_{\mathcal{X}}\}\}$ is the variance of the points on the trajectory and ensures that the error is the same for systems defined on different ranges of space. We found that SPE for invariant set localization was robust to sample size, exhibiting only a gradual increase in cycle error with increasing noise and decreasing number of observations, as can be seen in Figure 2 (right).

4.2. Classifying dynamical systems with prototype equivalence

We observed in Section 4.1 how matching a single prototype could be used to reconstruct an invariant set from sparse data. However, this demonstration relied on knowing that the observed system exhibited a particular invariant set. Can this information be discovered directly from data?

Here, we extend the previous results by fitting multiple prototypes and using loss residuals to classify input dynamics according to their invariant structures. As our prototype set, we choose all four effective systems implied by Equation (4), with $a = \pm \frac{1}{4}$ and $\omega = \pm \frac{1}{2}$. Four diffeomorphisms, H_k , were fit to data from each observed system in parallel and the one with the minimal value of the equivalence loss defined in Equation (2) was used to adjudicate class membership.

Table 1 shows the accuracy of our method averaged across observed systems, compared to existing baselines (Moriel et al., 2023): TWA, a convolutional framework that extracts topologically invariant features for classifying between periodic and point dynamical systems (Moriel et al., 2023); Critical Points, a heuristic approach that identifies critical points in the vector field (Helman & Hesselink, 1989; 1991); Lyapunov, a method that differentiates pre- and post-Hopf bifurcation states based on the Lyapunov exponent computed from a time series integrated from the vector field (Zhang et al., 2009); Phase2vec: a deep learning approach

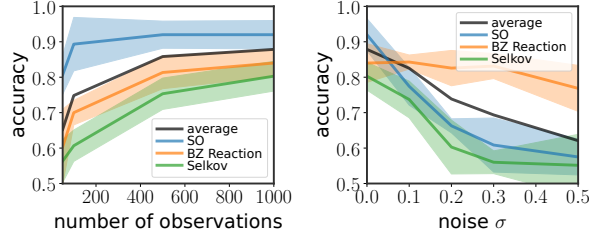


Figure 4. Classification accuracy as a function of the number of observed points (left) and amount of observation noise (right). The shaded areas for the different systems represent one standard deviation from the average, which is depicted by the solid line. The black line is the average accuracy over all systems (simple oscillator (SO), BZ reaction, Selkov, Liénard sigmoid, Liénard polynomial and Van der Pol).

for dynamical systems embedding, which learns vector field representations (Ricci et al., 2022); and Autoencoder, an autoencoder trained to reconstruct the vectors, whose latent code is used to classify the dynamics. To directly compare to all of these baselines, we classify systems with observations on a dense grid with $N = 4096$ observed points (x_i, \dot{x}_i) , although SPE is not restricted to this observations structure. SPE outperforms earlier baselines across all systems except for SO/Augmented SO (details in Appendix B.1), where TWA, which was fit to thousands of these systems using a dense grid of points in phase space, is slightly more performant (Table 1). Additionally, our approach’s use of prototypes with explicit diffeomorphisms means that, unlike competing methods, SPE can directly localize the invariant set (Section 4.1).

Furthermore, the SPE approach is robust to both noise and sample size. For example, when decreasing the number of sampled vectors per system to $N = 1000$ (25% of the points from the results in Table 1), we did not notice any significant dip in accuracy, as evidenced by the clean decision boundaries in Figure 3. We explored this effect systematically by tracking accuracy as a function of the number of observed vectors and the strength of additive Gaussian noise in the data set (Figure 4). We find only gradual decline in performance along these hyperparameters. Indeed, when we trained on as few as 50 random vectors, average accuracy was still relatively high, at 70%.

4.3. Beyond two dimensions

Real dynamical systems, or measurements thereof, are often embedded in high-dimensional spaces, even if their intrinsic behavior lies on a low-dimensional manifold (Champion et al., 2019). Classifying higher-dimensional systems and locating their invariant sets is a challenging problem since the classifier must also identify where are the lower-dimensional

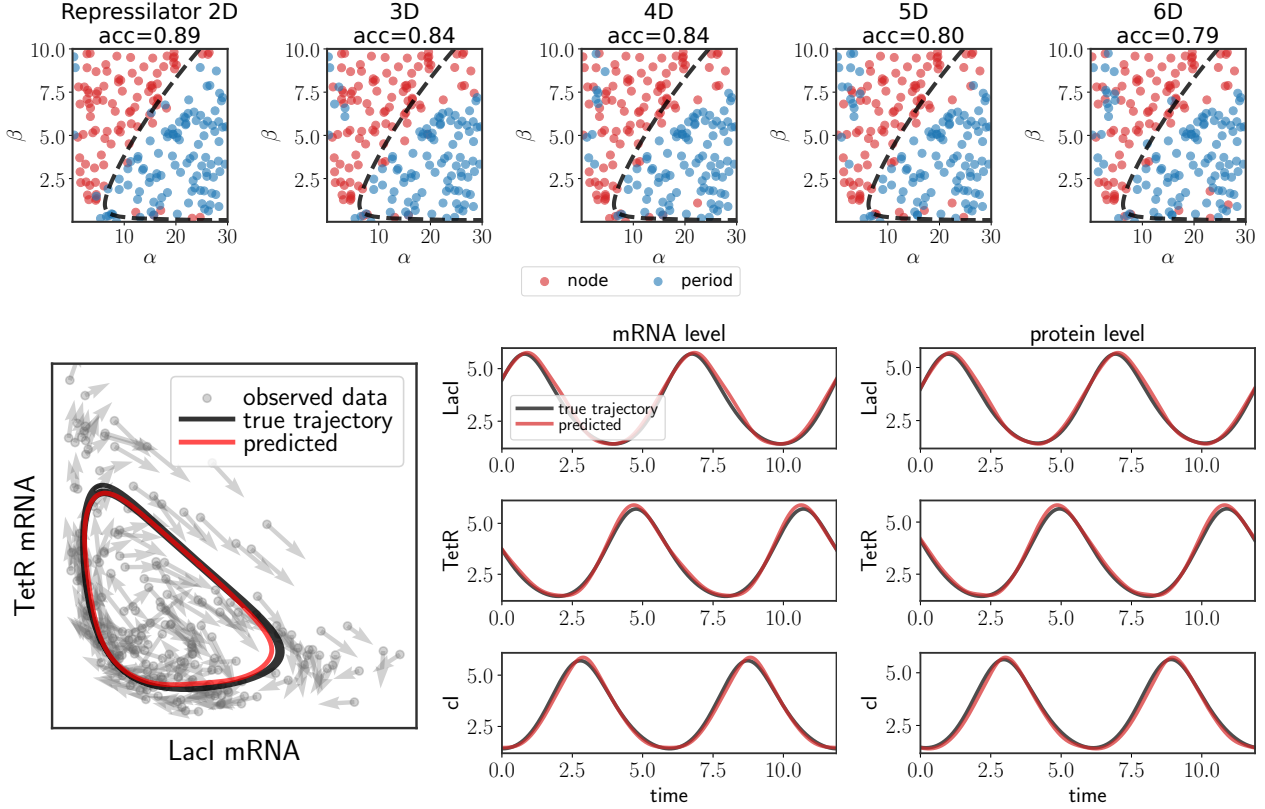


Figure 5. Classifying dynamics in higher dimensions and recovering the limit cycle from the repressilator system. **Top:** classification results using SPE on the repressilator system with $N = 1000$ observed vectors along a trajectory. Each point in the scatter represents a system with specific parameters that was classified by SPE as either a 2D embedded limit cycle (blue) or node attractor (red). The dashed black line depicts the ground truth bifurcation boundary between periodic and node behavior. Each column depicts dynamics projected onto a different dimensionality, with 2D in the left-most plot and the full 6D system in the right-most plot. Classification accuracy, averaged over all of the parameter settings considered, is written above each of the scatter plots. **Bottom:** qualitative results of fitting a 6-dimensional repressilator system, projected to the LacI-TetR mRNA plane (left). The gray arrows depict observed position-vector pairs, (x_i, \dot{x}_i) , the black line is the ground-truth invariant set of the dynamics and the red line is the predicted invariant set using SPE. Time series of the gene expression (center) and protein levels (right) can be extracted from the predicted limit cycle (shown in red). These are overlaid on top of a trajectory simulated from the underlying (hidden) system, which was simulated for a long time to ensure convergence to the limit cycle, shown in black.

dynamics of interest within this larger space.

Here, we show that our framework can easily adapt to the higher-dimensional case by combining prototype matching with dimensionality reduction. We assume that the invariant sets of the observed dynamics follow a 2-dimensional system embedded in a higher dimension. As such, we use prototypes that are the combination of two behaviors: (1) a 2D limit cycle/equilibrium behavior as before; (2) exponential decay to a fixed point along variables uncoupled from the embedded 2D system. Mathematically, we define these prototypes as:

$$\dot{y} = g_k(y) = \begin{bmatrix} g_{2D}^{(k)}(y_1), & -\tau \cdot y_2 \end{bmatrix}^T \quad (7)$$

with $y_1 \in \mathbb{R}^2$, $y_2 \in \mathbb{R}^{d-2}$, where $g_{2D}^{(k)}(\cdot)$ are velocities in two dimensions for the k -th prototype, and τ is a decay factor. We used $\tau = 1/2$ in all of our experiments.

We found that performance was improved by regularizing the diffeomorphism to map the data as close as possible to the embedded 2D dynamics. Essentially, if we assume that most of the observed dynamics are at or close to the invariant set of the prototype, then we expect the positions x_i to be close to a 2D manifold embedded in a higher dimension. Using the diffeomorphism, we can project the points onto the space containing the 2D invariant set, and then back into the observed space in the following way:

$$P(x; H_\theta) = H_\theta^{-1}([H_\theta(x)]_1, [H_\theta(x)]_2, 0, \dots, 0) \quad (8)$$

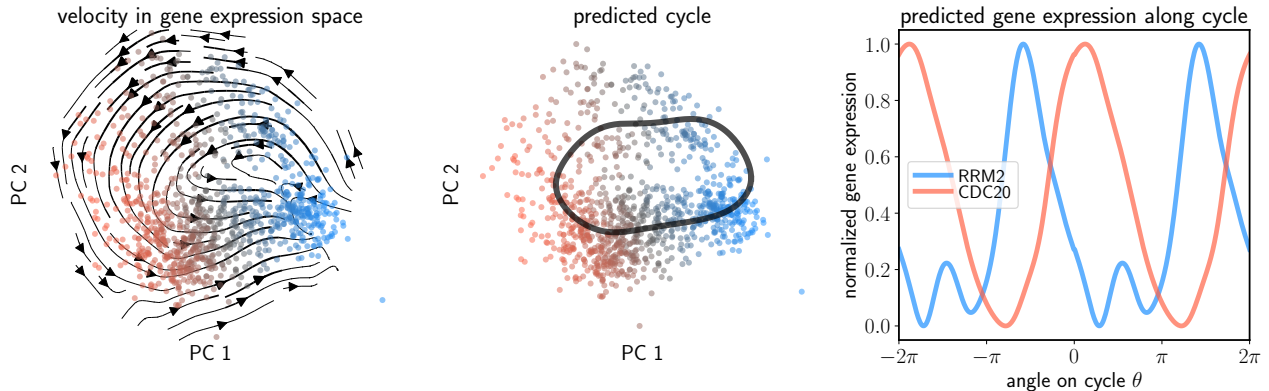


Figure 6. Recovering the cell cycle gene expression pattern from single-cell data. **Left:** gene expression velocity of cells undergoing proliferation in PCA space. Colors denote the cycle phase score based on marker gene expression; red corresponds to high expression of S-phase markers, blue to high expression of G2/M-phase genes, and gray corresponds to low expression levels of both. **Middle:** SPE was used to fit a periodic prototype to the RNA velocity data; its resulting cycle attractor is plotted in black. The cells’ locations and colors are as in the plot on the left. **Right:** predicted gene expression along the cycle attractor predicted by SPE. Specifically, the normalized expression is plotted vs. the angle on the limit cycle (θ), for the genes RRM2, a marker of S phase, and CDC20, a marker of G2/M phases. See details in Appendix C.

where $[H_\theta(x)]_i$ is the i -th coordinate of $H_\theta(x)$ and $P(x; H_\theta)$ denotes the projection according to $H_\theta(x)$.

We model the projection into data space through a Gaussian observation model, with the following loss added when training:

$$L_{\text{proj}}(H_\theta, \lambda_{\text{proj}}) = e^{\lambda_{\text{proj}}} \frac{1}{N} \sum_i \|x_i - P(x_i; H_\theta)\|^2 - \frac{1}{N} \lambda_{\text{proj}} \quad (9)$$

where λ_{proj} is the regularization coefficient, which takes the form of the log of the precision of the Gaussian observation model. Adding the regularization coefficient in this manner means that it can be optimized in parallel to the diffeomorphism, and allows for an adaptive fitting process. Modeling the projection in this way is similar to generative topographic mapping (GTM, (Bishop et al., 1998)) when the matching between the latent codes and the data is known. This projection loss was added to the loss defined in Section 3.1 for d -dimensional dynamics.

To test our approach in realistic higher-dimensional systems, we classify and localize invariant structures in data from the repressilator model of gene regulation (Elowitz & Leibler, 2000) (see Appendix B.3 for governing equations). The repressilator system is a model for a genetic regulatory network in bacteria, based on the mRNA and protein counts of three genes: TetR, LacI and λ phage cI. Each of these proteins inhibits the next gene, in a cyclic fashion, leading to oscillatory dynamics. The governing parameters for this system are related to the rates of the transcription, translation and degradation of the different genes and proteins. Even

though this system spans six dimensions, under specific parameter values it exhibits either a 2D point attractor or contains an embedded limit cycle (Verdugo, 2018a; Potvin-Trottier et al., 2016).

We use our framework to classify the dynamical regimes of repressilator systems with different rates of transcription α , and protein/mRNA degradation rates β , given 1000 observed vectors using the same sampling scheme for the data as described in Section 4.2, Figure 5. For lower dimensions we project the observed positions x_i and velocities \dot{x}_i onto a predefined subset of the six dimensions (for more details, see Appendix B.3). We observed (Figure 5) not only that our model could classify two-dimensional data better than earlier work (Moriel et al., 2023), but also that it could accurately distinguish equilibrium from cyclic behavior across all dimensionalities considered. As far as we are aware, classification of this kind carried out explicitly in higher dimensionalities is inaccessible using techniques from previous work. Moreover, our optimized diffeomorphisms in the six-dimensional case can be used to accurately locate the cyclic dynamics of the repressilator system, recapitulating the behavior of the system and its invariant set, as seen in Figure 5.

4.4. Uncovering the cell cycle expression pattern in single-cell data

Finally, we show how our method can be used to trace the periodic gene expression dynamics of real proliferating cells. The expression of cell-cycle genes follows a well-defined trajectory through different phases: initial growth

(G1), DNA replication (S phase), further growth (G2), and mitosis (M). Here, we analyze single-cell RNA-sequencing data from a human cell line, profiling over 50,000 genes across more than 1,000 cells (Mahdessian et al., 2021).

Previous approaches have inferred cell-cycle progression using marker genes (Tirosch et al., 2016), a learned projection (Zheng et al., 2022; Riba et al., 2022), or using structural priors (Schwabe et al., 2020; Karin et al., 2023), but these do not directly leverage the fact that the cycle has a characteristic dynamical structure in the form of a limit cycle. Indeed, we show that cell cycle structure can be estimated from RNA velocity (Bergen et al., 2021; Gorin et al., 2022), effective local velocities of cells in gene expression space that are based on differences in spliced and unspliced RNA counts.

Using the scVelo package (Bergen et al., 2020), we infer high-dimensional RNA velocities for all sampled cells and project them together with high-dimensional gene expression profiles of the cells, into a 10-dimensional space using principal component analysis (PCA). The resulting streamlines (Figure 6, left) reveal a noisy trajectory traversing across distinct S-phase and G2/M-phase gene expression states. We then fit a cyclic attractor to the RNA velocity data, capturing the periodic nature of the cell cycle (Figure 6, middle, see Appendix C for details).

Using the projection of the PCA, we can map the learned attractor back to gene expression space, revealing periodic, anti-correlated expression patterns of key cell-cycle marker genes such as RRM2 (S-phase) and CDC20 (G2/M-phase) (Figure 6, right). This demonstrates our method’s ability to recover biologically meaningful periodic processes directly from high-dimensional, noisy and sparse experimental data.

5. Discussion and future directions

In this work, we presented the smooth prototype equivalence (SPE) framework, a novel synthesis of prototype methods to identify and localize invariant structures in long-term dynamics given partial, sparse, and noisy observational data.

We envision several areas for future work. For example, we focused on cases where prototypes could be known in advance, but a challenging future direction would be the discovery of these prototypes directly from data. This would be especially relevant for cases where invariant structures change (via bifurcations) as a function of system parameters. Furthermore, we would be interested to extend our framework to new invariant structures, like strange attractors in chaotic systems (Lorenz, 1963). We are also interested in new biological applications, like detecting limit cycles in circadian gene networks to identify when stable oscillations emerge or break down under environmental or genetic perturbations.

Our method directly addresses challenges faced in scientific domains such as biology, climate science, and physics. By offering an equation-free approach for the detection of invariant sets like limit cycles and fixed points, our method has the potential to advance the understanding of complex, nonlinear processes in systems where traditional modeling is impractical.

Acknowledgments

We thank the Nitzan lab for their thoughtful feedback. This work was funded by the European Union (ERC, DecodeSC, 101040660) (M.N.). Views and opinions expressed are, however, those of the author(s) only and do not necessarily reflect those of the European Union or the European Research Council. Neither the European Union nor the granting authority can be held responsible for them.

References

- Andronov, A. A. and Pontryagin, L. S. Systèmes grossiers. *Doklady Akademii Nauk SSSR*, 14:247–251, 1937. Translated as “Rough Systems” in later works.
- Behrmann, J., Grathwohl, W., Chen, R. T., Duvenaud, D., and Jacobsen, J.-H. Invertible residual networks. In *International conference on machine learning*, pp. 573–582. PMLR, 2019.
- Bergen, V., Lange, M., Peidli, S., Wolf, F. A., and Theis, F. J. Generalizing rna velocity to transient cell states through dynamical modeling. *Nature biotechnology*, 38(12):1408–1414, 2020.
- Bergen, V., Soldatov, R. A., Kharchenko, P. V., and Theis, F. J. Rna velocity—current challenges and future perspectives. *Molecular systems biology*, 17(8):e10282, 2021.
- Bishop, C. M., Svensén, M., and Williams, C. K. Gtm: The generative topographic mapping. *Neural computation*, 10(1):215–234, 1998.
- Bonilla, E. and Robles-Kelly, A. Discriminative probabilistic prototype learning. *arXiv preprint arXiv:1206.4686*, 2012.
- Bramburger, J. J., Brunton, S. L., and Kutz, J. N. Deep learning of conjugate mappings. *Physica D: Nonlinear Phenomena*, 427:133008, 2021.
- Cavalu, S., Abdelhamid, A. M., Saber, S., Elmorsy, E. A., Hamad, R. S., Abdel-Reheim, M. A., Yahya, G., and Salama, M. M. Cell cycle machinery in oncology: A comprehensive review of therapeutic targets. *The FASEB Journal*, 38(11):e23734, 2024.

- Champion, K., Lusch, B., Kutz, J. N., and Brunton, S. L. Data-driven discovery of coordinates and governing equations. *Proc. Natl. Acad. Sci. U. S. A.*, 116(45):22445–22451, 2019.
- Chen, R., Vedovati, G., Braver, T., and Ching, S. Dform: Diffeomorphic vector field alignment for assessing dynamics across learned models. *arXiv preprint arXiv:2402.09735*, 2024.
- Chen, S., Hou, W., Hong, Z., Ding, X., Song, Y., You, X., Liu, T., and Zhang, K. Evolving semantic prototype improves generative zero-shot learning. In *Proceedings of the 40th International Conference on Machine Learning, ICML’23*. JMLR.org, 2023.
- Chervov, A. and Zinovyev, A. Computational challenges of cell cycle analysis using single cell transcriptomics. *arXiv [q-bio.QM]*, August 2022.
- Dimitriadis, G. *Introduction to nonlinear aeroelasticity*. John Wiley & Sons, 2017.
- Dinh, L., Krueger, D., and Bengio, Y. Nice: Non-linear independent components estimation. *arXiv preprint arXiv:1410.8516*, 2014.
- Durkan, C., Bekasov, A., Murray, I., and Papamakarios, G. Neural spline flows. *Advances in neural information processing systems*, 32, 2019.
- Elowitz, M. B. and Leibler, S. A synthetic oscillatory network of transcriptional regulators. *Nature*, 403(6767): 335–338, 2000.
- Ghadami, A. and Epureanu, B. I. Data-driven prediction in dynamical systems: recent developments. *Philosophical Transactions of the Royal Society A*, 380(2229):20210213, 2022.
- Ghafari-Fard, S., Khoshbakht, T., Hussien, B. M., Dong, P., Gassler, N., Taheri, M., Baniahmad, A., and Dilmaghani, N. A. A review on the role of cyclin dependent kinases in cancers. *Cancer Cell International*, 22(1):325, 2022.
- Glaz, B. Efficient pseudometrics for data-driven comparisons of nonlinear dynamical systems, 2024. URL <https://arxiv.org/abs/2409.18681>.
- Gorin, G., Fang, M., Chari, T., and Pachter, L. Rna velocity unraveled. *PLOS Computational Biology*, 18(9): e1010492, 2022.
- Grobman, D. M. Homeomorphisms of systems of differential equations. *Doklady Akademii Nauk SSSR*, 128: 880–881, 1959. English translation available in *Soviet Mathematics Doklady*, Vol. 1, 1960.
- Hartman, P. A lemma in the theory of structural stability of differential equations. *Proceedings of the American Mathematical Society*, 11(4):610–620, 1960. doi: 10.2307/2034363.
- Helman, J. and Hesselink, L. Representation and display of vector field topology in fluid flow data sets. *Computer*, 22(08):27–36, 1989.
- Helman, J. L. and Hesselink, L. Visualizing vector field topology in fluid flows. *IEEE Computer Graphics and Applications*, 11(3):36–46, 1991.
- Hilbert, D. Mathematical problems. *Bulletin of the American Mathematical Society*, 8(10):437–479, 1902. doi: 10.1090/S0002-9904-1902-08860-7. URL <https://www.ams.org/journals/bull/1902-08-10/S0002-9904-1902-08860-7/>.
- Karin, J., Bornfeld, Y., and Nitzan, M. scPrisma infers, filters and enhances topological signals in single-cell data using spectral template matching. *Nat. Biotechnol.*, February 2023.
- Kingma, D. P. Adam: A method for stochastic optimization. *arXiv preprint arXiv:1412.6980*, 2014.
- Lorenz, E. N. Deterministic nonperiodic flow. *Journal of the Atmospheric Sciences*, 20(2):130–141, 1963. doi: 10.1175/1520-0469(1963)020<0130:DNF>2.0.CO;2.
- Mahdessian, D., Cesnik, A. J., Gnann, C., Danielsson, F., Stenström, L., Arif, M., Zhang, C., Le, T., Johansson, F., Schutten, R., et al. Spatiotemporal dissection of the cell cycle with single-cell proteogenomics. *Nature*, 590(7847):649–654, 2021.
- Moriel, N., Ricci, M., and Nitzan, M. Let’s do the time-warp-attend: Learning topological invariants of dynamical systems. *arXiv preprint arXiv:2312.09234*, 2023.
- Morse, M. and Hedlund, G. A. Symbolic dynamics. *American Journal of Mathematics*, 60(4):815–866, 1938. doi: 10.2307/2371264.
- Nayfeh, A. H. *The Method of Normal Forms*. John Wiley & Sons, 2008.
- Novák, B. and Tyson, J. J. Design principles of biochemical oscillators. *Nature reviews Molecular cell biology*, 9(12): 981–991, 2008.
- Papamakarios, G., Nalisnick, E., Rezende, D. J., Mohamed, S., and Lakshminarayanan, B. Normalizing flows for probabilistic modeling and inference. *Journal of Machine Learning Research*, 22(57):1–64, 2021.

- Poincaré, H. *Les Méthodes Nouvelles de la Mécanique Céleste*, volume 1–3. Gauthier-Villars, Paris, France, 1892–1899. Available as a reprint from Dover Publications, 1957.
- Potvin-Trottier, L., Lord, N. D., Vinnicombe, G., and Paulsson, J. Synchronous long-term oscillations in a synthetic gene circuit. *Nature*, 538(7626):514–517, 2016.
- Redman, W. T., Fonoberova, M., Mohr, R., Kevrekidis, I. G., and Mezić, I. Algorithmic (semi-)conjugacy via koopman operator theory, 2022. URL <https://arxiv.org/abs/2209.06374>.
- Riba, A., Oravec, A., Durik, M., Jiménez, S., Alunni, V., Cerciati, M., Jung, M., Keime, C., Keyes, W. M., and Molina, N. Cell cycle gene regulation dynamics revealed by rna velocity and deep-learning. *Nature communications*, 13(1):2865, 2022.
- Ricci, M., Moriel, N., Piran, Z., and Nitzan, M. Phase2vec: Dynamical systems embedding with a physics-informed convolutional network. *arXiv preprint arXiv:2212.03857*, 2022.
- Rosch, E. H. Natural categories. *Cognitive psychology*, 4(3):328–350, 1973.
- Schwabe, D., Formichetti, S., Junker, J. P., Falcke, M., and Rajewsky, N. The transcriptome dynamics of single cells during the cell cycle. *Mol. Syst. Biol.*, 16(11):e9946, November 2020.
- Skufca, J. D. and Bollt, E. M. Relaxing conjugacy to fit modeling in dynamical systems. *Phys. Rev. E*, 76:026220, Aug 2007. doi: 10.1103/PhysRevE.76.026220. URL <https://link.aps.org/doi/10.1103/PhysRevE.76.026220>.
- Skufca, J. D. and Bollt, E. M. A concept of homeomorphic defect for defining mostly conjugate dynamical systems. *Chaos: An Interdisciplinary Journal of Nonlinear Science*, 18(1):013118, 2008.
- Smale, S. Mathematical problems for the next century. *Mathematics: frontiers and perspectives*, pp. 271–294, 2000.
- Sternberg, S. Local contractions and a theorem of poincaré. *American Journal of Mathematics*, 79(4):809–824, 1957. doi: 10.2307/2372447.
- Sternberg, S. On the structure of local homeomorphisms of euclidean n -space, II. *American Journal of Mathematics*, 86(2):258–292, 1964. doi: 10.2307/2373158.
- Suski, J. M., Braun, M., Strmiska, V., and Sicinski, P. Targeting cell-cycle machinery in cancer. *Cancer cell*, 39(6):759–778, 2021.
- Takens, F. Detecting strange attractors in turbulence. In Rand, D. A. and Young, L.-S. (eds.), *Dynamical Systems and Turbulence, Warwick 1980*, volume 898 of *Lecture Notes in Mathematics*, pp. 366–381. Springer-Verlag, Berlin, Heidelberg, 1981. doi: 10.1007/BFb0091924.
- Tirosh, I., Izar, B., Prakadan, S. M., Wadsworth, M. H., Treacy, D., Trombetta, J. J., Rotem, A., Rodman, C., Lian, C., Murphy, G., et al. Dissecting the multicellular ecosystem of metastatic melanoma by single-cell rna-seq. *Science*, 352(6282):189–196, 2016.
- Verdugo, A. Hopf bifurcation analysis of the repressilator model. *American Journal of Computational Mathematics*, 8(02):137–152, 2018a.
- Verdugo, A. Hopf bifurcation analysis of the repressilator model. *American Journal of Computational Mathematics*, 8(2):137–152, 2018b.
- Weisshaar, T. A. Aeroelasticity, an introduction to fundamental problems-with an historical perspective, examples and homework problems, 2012.
- Zhang, J.-G., Li, X.-F., Chu, Y.-D., Yu, J.-N., and Chang, Y.-X. Hopf bifurcations, lyapunov exponents and control of chaos for a class of centrifugal flywheel governor system. *Chaos, Solitons & Fractals*, 39(5):2150–2168, 2009.
- Zheng, S. C., Stein-O’Brien, G., Augustin, J. J., Slosberg, J., Carosso, G. A., Winer, B., Shin, G., Bjornsson, H. T., Goff, L. A., and Hansen, K. D. Universal prediction of cell-cycle position using transfer learning. *Genome Biol.*, 23(1):41, January 2022.
- Zheng, S. C., Stein-O’Brien, G., Boukas, L., Goff, L. A., and Hansen, K. D. Pumping the brakes on rna velocity by understanding and interpreting rna velocity estimates. *Genome biology*, 24(1):246, 2023.

A. Diffeomorphism details

The diffeomorphisms $H : \mathcal{X} \rightarrow \mathcal{Y}$ used in this work are normalizing flows with alternating *Affine* and *Fourier Feature Coupling* (FFCoupling) transforms, both of which are explained in further details below. Furthermore, the first layer of the normalizing flow was set to standardize the data, effectively an *ActNorm* layer (Papamakarios et al., 2021), defined as:

$$[\text{ActNorm}(x)]_i = \frac{x_i - \text{mean}(x_i)}{\text{std}(x_i)} \quad (10)$$

In the above, $\text{mean}(x_i)$ and $\text{std}(x_i)$ are the mean and standard deviations of i -th coordinate of the observed data, respectively. This ActNorm layer was kept frozen after initialization, and means that the normalization of the data is explicitly part of the learned diffeomorphism.

A.1. Fourier feature coupling

The FFCoupling layer we used is a modification of the standard *AffineCoupling* (Papamakarios et al., 2021; Dinh et al., 2014) layer used in normalizing flows. *AffineCoupling* splits an input x to two sub-vectors x_1 and x_2 , and the transformation itself is defined as:

$$\begin{bmatrix} y_1 \\ y_2 \end{bmatrix} = \text{AffineCoupling}(x) = \begin{bmatrix} x_1 \\ \exp[f_s(x_1)] \circ x_2 + f_t(x_1) \end{bmatrix} \quad (11)$$

where $f_s(\cdot)$ is a scaling function, $\exp[f_s(\cdot)]$ is the element-wise exponent of $f_s(\cdot)$, $f_t(\cdot)$ is a translation function, and \circ stands for element-wise multiplication. *AffineCoupling* is defined in this manner to ensure invertibility, in which case $f_s(\cdot)$ and $f_t(\cdot)$ can be arbitrarily complex functions. These two functions are typically parameterized by a multi-layer perceptron (MLP). Baked into the *AffineCoupling* transformation is the simple form of its log-determinant:

$$\log |\text{AffineCoupling}(x)| = \sum_i [f_s(x_1)]_i \quad (12)$$

Finally, note that *AffineCoupling* only transforms x_2 as a function of x_1 . To account for this, it is standard to chain two transformations, one where x_1 acts on x_2 and another with the roles reversed. For simplicity, we regard such a chaining of two *AffineCoupling* transformations as a single layer.

Unfortunately, when both the scale and the translation functions are defined as MLPs, calculating the Jacobian or Jacobian-vector products (JVPs) is not straightforward. These JVPs are needed for our loss (Equation (2)) and can potentially be found using autograd methods, albeit at a high computational cost. Furthermore, we expect these diffeomorphisms to typically be quite smooth and act on a range of frequencies, properties which are not easily enforced in MLPs. Instead, we opt to use transformations whose JVPs can be calculated in closed-form and whose properties are well understood.

For our scale and translation functions we use the following *FFCoupling*:

$$\mathcal{F}(x) = \sum_{k=1}^K \Theta_k \cos\left(\frac{2\pi}{R}k \cdot x + \phi_k\right) \quad (13)$$

where $\cos(x)$ is an element-wise cosine. As defined, the frequency coefficients $\Theta_k \in \mathbb{R}^{d \times d}$ and phases $\phi_k \in \mathbb{R}^d$ are learnable parameters, while the number of frequencies K and the range R are hyperparameters. When K is large, this transformation is expressive enough to fit any function defined in the range $[-R/2, R/2]$. It also admits a very simple form for the Jacobian, given by:

$$\frac{\partial}{\partial x} \mathcal{F}(x) = -\frac{2\pi}{R} \sum_k k \cdot \Theta_k \text{diag}\left[\sin\left(\frac{2\pi}{R}k \cdot x + \phi_k\right)\right] \quad (14)$$

A.2. Affine transformation layer

Besides the FFCoupling layer, we also use affine transformations. To ensure invertibility, we parameterize this transformation as:

$$\text{Affine}(x) = WW^T x + e^\varphi \cdot x + \mu \quad (15)$$

where $W \in \mathbb{R}^{d \times q}$ with some chosen q , $\varphi \in \mathbb{R}$ and $\mu \in \mathbb{R}^d$ are learnable parameters. This factorization ensures that the matrix $WW^T + Ie^\varphi$ is positive-definite (PD), and thus invertible. It also enables closed-form inversion using the matrix-inversion lemma.

A.3. Network and Training Specifications

As mentioned above, the normalizing flow we use have alternating Affine and FFCoupling transforms. A single block of our network is defined as Affine \rightarrow FFCoupling \rightarrow ReverseFFCoupling, where the ReverseFFCoupling switches the roles of x_1 and x_2 , as explained in Appendix A.1. We use 4 such blocks for our normalizing flows, where:

- The number of frequencies in the FFCoupling is $K = 5$
- The range of the FFCoupling is chosen to be $R = 10$
- The rank of the Affine transformation in each block is after the first one is $q = 2$, so that $W \in \mathbb{R}^{d \times 2}$

Before these blocks, our networks include a frozen ActNorm layer that standardizes the data and ensures that all learned diffeomorphism have similar inputs, and then a full-rank Affine transformation, with learnable weights.

Training is carried out using the Adam optimizer (Kingma, 2014) with a learning rate and weight decay of 0.001. Beyond these, we used two additional regularization functions:

- **Determinant regularization:** we found it beneficial to regularize the log-determinant to be close to 0. For all experiments except for the cell-cycle data (see more details in Appendix C), the regularization coefficient used was $\lambda_{\text{det}} = 10^{-3}$.
- **Center regularization:** when the observations are very noisy, the learned transformations can converge to a local minima with the center of the prototype very far from the data. To alleviate this problem, we add a center regularization, which penalizes transformations that send the focal point of the prototype to be very far from the mean of the observed data. For all experiments except for the cell-cycle data, the regularization coefficient used was $\lambda_{\text{cent}} = 10^{-6}$.

The full loss is given by:

$$L(H_\theta) = L_E(H_\theta, g) + \lambda_{\text{det}} \left| \frac{1}{N} \sum_i \det [\partial_x H_\theta(x_i)] \right| + \lambda_{\text{cent}} \|\bar{x} - H_\theta^{-1}(0)\|^2 + L_{\text{proj}}(H_\theta, \lambda_{\text{proj}}) \quad (16)$$

where $L_{\text{proj}}(H_\theta, \lambda_{\text{proj}})$ is as defined in Section 4.3. For high-dimensional data, the projection log-precision was initialized as $\lambda_{\text{proj}} = -1$.

A.4. Normalizing Flows and Orientations

In applications of normalizing flows, it is common to parameterize the layers of the normalizing flow such that they have a positive determinant. While negative determinants do not mean that the transformation will not be invertible, it is impossible to use gradient descent (GD) transition from transformations with positive determinants to those with negative determinants. Specifically, to get from a parametric space with a positive determinant to one with a negative determinant, the GD algorithm must be able to pass arbitrarily close to a transformation with a determinant equal to zero. That is, using GD means that to move from transformations with positive determinant to those with negative determinant, GD must always pass through the space of singular transformations, which are not invertible by definition.

The consequence in our application is that the trained positive determinant normalizing flow cannot flip the orientation of space about an axis, i.e. the transformation $x_i = -x_i$ in any dimension i cannot be learned using our parameterization. For example, there exists no normalizing flow with a positive determinant between a clockwise and counter-clockwise limit cycle. For this reason we opt to use 4 different prototypes in Section 4.2, a node and a cycle for each of the two (clockwise and counter-clockwise) orientations.

When the diffeomorphisms are defined on a higher-dimensional space, the diffeomorphisms can essentially flip orientation. This is possibly due to the choice of prototypes we used in high dimensions, and due to the fact that the data lies on a low-dimensional manifold within the ambient space. When the transformation is expressive enough, it can fold space using the transient dimensions of our prototypes, to seemingly flip the orientation of the low-dimensional dynamics. That said, in practice we still use the same 4 prototypes in higher-dimensional spaces.

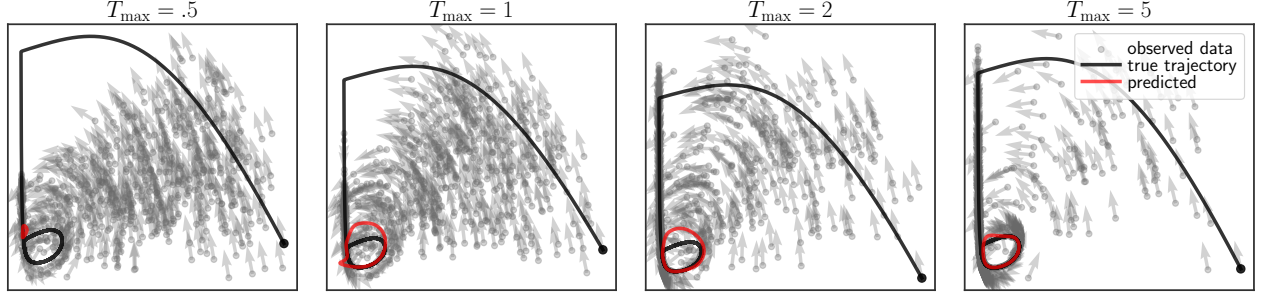


Figure 7. The effects of changing the maximum simulation sampling time T_{\max} . When T_{\max} is small (e.g. $T_{\max} = 0.5$; left), most of the observations are transients. On the other hand, when T_{\max} is large (e.g. $T_{\max} = 5$; right), most of the observations are on the invariant set.

B. Simulation details

B.1. 2D systems

For the 2D simulated dynamics, we use the same systems as in [Moriel et al.](#). The governing equations for these systems are shown in Table 2 (adapted from [Moriel et al. 2023](#)). We additionally study the *Augmented SO* system, which is an instance

System Name	Equation	Phase space	Parameter ranges
Simple Oscillator (SO)	$\dot{r} = r(a - r^2); \dot{\theta} = \omega$	$x_1, x_2 \in [-1, 1]$	$a \in [-0.5, 0.5], \omega \in [-1, 1]$
Liénard Polynomial	$\dot{x}_1 = x_2; \dot{x}_2 = -(ax_1 + x_1^3) - (c + x_1^2)x_2$	$x_1, x_2 \in [-4.2, 4.2]$	$a \in [0, 1], c \in [-1, 1]$
Liénard Sigmoid	$\dot{x}_1 = x_2; \dot{x}_2 = -(1/(1 + e^{-ax_1}) - 0.5) - (b + x_1^2)x_2$	$x_1, x_2 \in [-1.5, 1.5]$	$a \in [0, 1], b \in [-1, 1]$
Van der Pol	$\dot{x}_1 = x_2; \dot{x}_2 = \mu x_2 - x_1 - x_1^2 x_2$	$x_1, x_2 \in [-3, 3]$	$\mu \in [-1, 1]$
BZ Reaction	$\dot{x}_1 = a - x_1 - \frac{4x_1 x_2}{1+x_1^2}; \dot{x}_2 = bx_1 \left(1 - \frac{x_2}{1+x_1^2}\right)$	$x_1, x_2 \in [0, 20]$	$a \in [2, 19], b \in [2, 6]$
Selk'ov	$\dot{x}_1 = x_1 + ax_2 + x_1^2 x_2; \dot{x}_2 = b - ax_2 - x_1^2 x_2$	$x_1, x_2 \in [0, 3]$	$a \in [0.01, 0.11], b \in [0.02, 1.2]$

Table 2. Governing equations, range of phase space and range of parameters for simulated systems, adapted from [Moriel et al. 2023](#).

of a simple oscillator (SO) that was transformed by a random initialization of a neural spline flows ([Durkan et al., 2019](#)). All of these systems change behavior from node attractors to limit cycles, i.e. undergo a Hopf bifurcation, at known parametric settings, making them particularly relevant for our application.

B.2. Simulating sparse data

The most straightforward method to draw sparse data from each system is to draw points uniformly from the phase-space. However, for high-dimensional systems this runs the risk of under-sampling the region of the invariant set, observations which we require in order to make any meaningful prediction. Moreover, this does not accurately portray how we expect data to be collected in real scenarios. Instead, we assume that each point of the data is a point on a random trajectory, with initial conditions coming from a uniform distribution on pre-specified ranges of the phase-space. Additionally, we assume that each observed pair (x_i, \dot{x}_i) has independently traversed a different amount of time on its respective trajectories. The data sampling process can be summarized through the following steps:

1. For each $i \in \{1, \dots, N\}$, draw the initial conditions $x_i^{(0)}$ uniformly from a pre-specified portion of space
2. Sample the amount of time t_i uniformly in the range $[T_{\min}, T_{\max}]$
3. Simulate a trajectory beginning at $x_i^{(0)}$ to time t_i . The point x_i reached on the trajectory in this manner is defined as the position, and $\dot{x}_i = f(x_i)$ as the velocity
4. Optionally, Gaussian noise with standard deviation σ is then added to \dot{x}_i

Usually we set the parameter $T_{\min} = 0$, except when sampling from the repressilator (see Appendix B.3 for more

information). T_{\max} is a hyper-parameter that effectively controls how much samples tend to concentrate around the invariant set. When T_{\max} is close to 0, then the pairs (x_i, \dot{x}_i) revert back to being uniformly sampled from phase-space.

An example of the effect of different values for T_{\max} can be seen in Figure 7. When T_{\max} is small, the observations mostly include transients of the dynamics, in which case not much can be estimated with regards to the invariant set of the system. As T_{\max} increases, more points aggregate near the invariant set. For our 2D simulations we use $T_{\max} \approx 3$.

B.3. Repressilator

The repressilator system is governed by six coupled differential equations, structured as three instances of the following gene-regulation model (Elowitz & Leibler, 2000):

$$\begin{aligned} \dot{m}_i &= -m_i + \frac{\alpha}{1 + p_j^n} + \alpha_0, \\ \dot{p}_i &= -\beta(p_i - m_i), \end{aligned}$$

where m_i and p_i denote the mRNA and protein concentrations for gene i , corresponding to **LacI**, **TetR**, and λ **cI**, with cyclic inhibition: $i = \text{LacI, TetR, cI}$ and $j = \text{cI, LacI, TetR}$. The parameters α_0 (basal transcription), α (maximal transcription), β (protein/mRNA degradation ratio), and n (Hill coefficient) define the system’s regulatory dynamics.

We analyze trajectories across $\alpha \in (0, 30)$, $\beta \in (0, 10)$, with $\alpha_0 = 0.2$, $n = 2$. A supercritical Hopf bifurcation emerges at critical values of β (Verdugo, 2018b):

$$\begin{aligned} \beta_1 &= \frac{3A^2 - 4A - 8}{4A + 8} + \frac{A\sqrt{9A^2 - 24A - 48}}{4A + 8}, \\ \beta_2 &= \frac{3A^2 - 4A - 8}{4A + 8} - \frac{A\sqrt{9A^2 - 24A - 48}}{4A + 8}, \end{aligned}$$

where

$$A = \frac{-\alpha n \hat{p}^{(n-1)}}{(1 + \hat{p}^n)^2}, \quad \hat{p} = \frac{\alpha}{1 + \hat{p}^n} + \alpha_0$$

We plot these boundaries in Figure 5.

To simulate instances of the repressilator, we use the same sampling procedure as described in Appendix B.2, with $T_{\min} = 3$ and $T_{\max} = 10$. In this context we use $T_{\min} = 3$ to ensure that when the samples are projected to lower than six dimensions they still define a vector field with non-intersecting trajectories. Furthermore, even though we used $T_{\max} = 10$, a larger value than in the other simulated systems, we found that the observed points do not all lie on the invariant set of the repressilator.

C. Identification of the cell cycle trajectory from single-cell RNA-sequencing and RNA velocity data of proliferating cells

We analyzed single-cell RNA-sequencing data from U2OS cell line that was integrated with the fluorescent ubiquitination-based cell cycle indicator (FUCCI) in order to investigate the spatiotemporal dynamics of human cell cycle expression (data collected in (Mahdessian et al., 2021)). The original dataset included 1,152 cells characterized by the expression of 58,884 genes. After preprocessing, following the protocol in Zheng et al. (2023)—which involved gene and cell filtering, normalization, log transformation, and the selection of highly variable genes, with a particular emphasis on cell cycle-associated genes identified by Tirosh et al. (2016)—1,021 cells remained, described by 54 genes.

To infer local measures of cellular dynamics in the high-dimensional gene expression space, we used scVelo (Bergen et al., 2020) which computes RNA velocity vectors from spliced and unspliced gene expression counts of a cell population. scVelo models the transcriptional dynamics of each gene using a dynamical model of transcription, splicing, and degradation. It applies an Expectation-Maximization algorithm to estimate gene-specific kinetic parameters and to infer the latent transcriptional state of each cell.

The gene expression data and the inferred velocities were projected into a 10-dimensional space using principal component analysis (PCA). Streamlines of the resulting velocity field are visualized in Figure 6, left. Independently of the RNA velocities, we computed S-phase and G2/M-phase scores per cell by aggregating the expression of marker genes for these phases, as defined by Tirosh et al. (2016), using the function “score_genes_cell_cycle” from scVelo package (Bergen et al., 2020). The color in Figure 6, left and middle, represents the fractional component of the S-phase score relative to the combined S and G2/M scores.

We then applied our method to fit the RNA velocities, embedded in the 10-dimensional PCA space, to a 10-dimensional cyclic SO prototype. This prototype oscillates in the first two dimensions and decays exponentially in the others. The fitting parameters were as follows: SO angular speed $\omega = 5$, radius $a = 1$, four blocks as defined in Appendix A, $K = 3$ frequencies per layer, weight decay of 0.001, projection regularization set to 0.01, center regularization of 0.001, a learning rate of 0.001, and 1,000 iterations. For details refer to Section 4.3.

To avoid convergence to local optima, we applied curriculum training where we gradually increased the complexity of the fitted diffeomorphism. Initially, we trained only the affine transformation layers, which captured the general region of the cell cycle but lacked the ability to model non-linear deformations. After completing half of the training iterations, we unfroze the parameters of the FFCoupling layers, allowing the model to capture complex non-linear transformations of the limit cycle.

To make the optimization robust to outliers, we considered only the 40% of the cells that were closest to the prototype’s limit cycle. To do this, at each iteration all points were transformed using the diffeomorphism and only the 40% with the smallest norm were selected for fitting. We found that this allowed the diffeomorphism to effectively focus only on cells relevant for the limit cycle, ensuring a more accurate fit.

Finally, given the fitted coordinates of the cycle attractor in the 10-dimensional PCA space, we inverted the PCA transformation to reconstruct the corresponding predicted gene expression. In Figure 6, we plot representative marker genes for both the S-phase and G2/M-phase, showing distinct oscillatory patterns consistent with cell cycle progression.